Journal of Membrane Science 437 (2013) 25–32

Contents lists available at SciVerse ScienceDirect

Journal of Membrane Science

journal homepage: www.elsevier.com/locate/memsci

Experimental validation of computational models for mass transport through micro heterogeneous membranes

Marco Dondero, Adrián P. Cisilino, J. Pablo Tomba *

Institute of Materials Science and Technology (INTEMA), National Research Council (CONICET), National University of Mar del Plata (UNMDP), Juan B. Justo 4302, (7600) Mar del Plata, Argentina

ARTICLE INFO

Article history:
Received 10 September 2012
Received in revised form
15 February 2013
Accepted 19 February 2013
Available online 27 February 2013

Keywords:
Mass transport
Confocal Raman microscopy
Boundary elements
Barrier membrane

ABSTRACT

This work describes a setup for the experimental and theoretical study of the mass transport of a penetrant through a two-dimensional model-material microstructure consisting in a homogeneous matrix with slender obstacles. Experiments were performed using polydimethylsiloxane (PDMS) specimens with a controlled pattern of randomly distributed laser-ablated microscopic slender holes that mimic the obstacles to the diffusion of the penetrant, 1-octadecanol (ODOL). Mass transport of ODOL throughout the patterned PDMS matrix was monitored by means of Confocal Raman microscopy. Rigorous numerical simulations of ODOL transport in transient regime were performed using the Boundary Element Method for exactly the same model-material microstructure topology used in the experimental tests. It was found that both, experiments and BEM simulations very well capture local barrier effects of the obstacles to the ODOL transport. The whole strategy provides a valuable base for validation and experimental verification of theoretical models of mass transport through heterogeneous membranes with complex barrier structure.

© 2013 Elsevier B.V. All rights reserved.

1. Introduction

The control of transport properties through heterogeneous systems has technological importance in many polymeric-based materials such as foams, blends and composites. Mass transport is particularly relevant in composites obtained by addition of layered silicates with dimensions in the nanometer scale (nanoclays) to a polymer matrix. This family of materials, referred in the literature to as nanocomposites, has shown dramatic improvements in, for instance, gas barrier properties, with very low volume fraction of fillers (below 5%), which can be exploited in applications such as coatings, packaging and controlled drug release, among others.

The barrier effect in nanocomposite materials can be rationalized in terms of the increment in path length experienced by the penetrant as it moves through the polymer matrix in the presence of the physical barriers imposed by the filler [1]. On a finer scale, the penetrant may also interact with the filler altering its mass transport coefficient compared with that in the neat matrix [2]. At this point, characteristics of the barriers such as length-to-thickness ratio, volume fraction, orientation and state of aggregation are expected to affect the overall transport behavior of the composite system. Several models have been proposed to describe the reduction of permeability in composite systems in terms of the increased path length or tortuosity. A recent review summarizes many of them [3]. Most of the models assume that the barriers have a regular and uniform shape, with some specific, ordered or random, spatial distribution [1]. The penetrant trajectory is idealized as a one-dimensional path which experiments abrupt changes in direction when the penetrant encounters a barrier, see Fig. 1. This family of simple models uses the so-called tortuosity factors to account for the effects of aspect ratio, volume fraction and aggregation of barriers on diffusivity or permeability [1,4]. As these models typically yield closed formulas for the apparent membrane permeability, we may refer to them as analytical.

Over the last years, the field of computational modeling of materials has experienced a sustained progress. High performance numerical methods such as Boundary Elements (BEM) and Finite Elements (FEM) have made possible numerical simulations of heat and mass transport for fairly complex material microstructures. The advantage of computational models is that the actual material structure can be described in detail. Thus, the effects of shape, size, orientation and spatial distributions of every phase can be precisely accounted for with much more precision than in above-mentioned analytical models [5–7]. With a continuously spreading use in material science, computational modeling has turn into a valuable tool to assist materials development. For instance, the combination of computational modeling with optimization algorithms allows for the design of the

* Corresponding author. Tel.: +54 0223 4816600.
E-mail address: jptomba@fi.mdp.edu.ar (J. Pablo Tomba).

0376-7388/$ - see front matter © 2013 Elsevier B.V. All rights reserved.
http://dx.doi.org/10.1016/j.memsci.2013.02.039

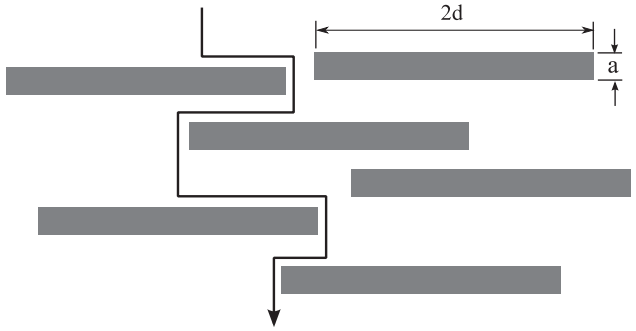

Fig. 1. Idealized barrier effect showing the increment in the diffusion path of a molecule as it encounters the impenetrable barriers.

material micro/nanostructure in order to achieve a customized set of macroscopic transport properties [8–10].

On the experimental side, some efforts are still needed, particularly in terms of the design of reliable systems for model validation. The limitation is not related with the availability of suitable experimental techniques but with the ability to control and/or characterize the material structure in order to match that represented in computer simulations. The possibility of generating model materials with well-defined and easily controlled structural features appears as a first necessary step to be considered for model validation. This strategy was first explored by Liu and Cussler [11], who used lithographically printed membranes with well-defined (regular) barrier structures to carry out experiments that served to test the basis of some of the most representative analytical models for mass transport.

We propose in this work an experimental setup and a measurement procedure devised to monitor the mass transport of a penetrant through a two-dimensional model-material microstructure consisting of a homogeneous matrix with a random distribution of slender obstacles. The system has been conceived as a benchmark test for the validation of numerical BEM predictions for the penetrant diffusion throughout the material microstructure in transient regime, with no constraints in terms of phase size, amount, or distribution. The matrix is made from cross-linked poly(dimethylsiloxane) (PDMS), with the obstacles mimicked via a controlled pattern of randomly-placed laser-ablated microscopic slender holes. The holes, which perform as impenetrable barriers, hinder the mass transport of the penetrant, 1-octadecanol (ODOL). Mass transport of ODOL through the microstructure is monitored by means of Confocal Raman microscopy, a technique that allows chemical discrimination between components with sub-micrometer spatial resolution. With this technique, we can directly determine a map of ODOL concentration throughout the patterned samples, which can be in turn contrasted with the numerical results obtained by BEM simulations.

2. System design

To facilitate measurements and comparison with calculations, the experimental setup has been designed in accordance to the following five basic pre-requisites:

i. The diffusion has to be two-dimensional, this is, the mass transport in the direction of the specimen thickness should be negligible;
ii. The matrix has to be patternable at micron level;
iii. The geometry and microstructure topology has to be easily tailored at the experimental scale;
iv. Mass transport of penetrant in the matrix has to be described by a single diffusion coefficient, preferably in the range 10^{-6}–10^{-8} cm^2/s;
v. Diffusion has to be virtually suppressed at room temperature to facilitate the micro-spectroscopic characterization of the specimen.

The material matrix is PDMS, which was chosen because is patternable by a variety of methods, including soft lithography and laser ablation. A microstructure of holes with slender shape, and specific positions, orientations and volume fraction is used to mimic the effect of the obstacles on mass transport, see Fig. 2.

The holes are patterned in the PDMS matrix by laser ablation. Depending on how finely the laser is focused on the sample, patterned features below 10 μm have been reported using this technique [12]. Soft lithography was also considered, but it was discarded because it requires a series of somewhat complicated steps to produce the desired pattern [13]. On the contrary, laser ablation can be directly carried out on the preformed matrix in a single step.

The diffusing molecule is ODOL, a long chain alcohol. The diffusion of ODOL in PDMS is expected to be mostly Fickean, as cross-linked PDMS behaves essentially as a viscous liquid above its glass transition temperature (~ -100 °C). Moreover, as the melting point of the alcohol molecule is about 57 °C, ODOL diffusion can be virtually stopped by freezing when the system is cooled at room temperature, and then further activated by heating above 57 °C. By supplying ODOL molecules from a reservoir located at one of the specimen ends, see Fig. 2, diffusion should proceed through the obstacle field given by the preformed holes. Initially, diffusion should be driven by the concentration gradient in *y*-direction, to become bi-dimensional (*xy*) as soon as ODOL molecules encounter the obstacles. As the features to be spatially resolved are on the micron scale, confocal Raman microscopy is used for the measurements. Besides, the differences between the chemical structures of the PDMS and ODOL molecules are expected to provide enough spectral contrast to be individually identified and spatially resolved throughout the specimen.

2.1. Experimental

PDMS networks were prepared from a commercial formulation, Sylgard 184 (Dow Corning, Midland, USA). 1-octadecanol (ODOL) was obtained from Aldrich (Japan) and used as received. Specimens were prepared as follows. First, a thin PDMS film, 200 μm thick, was synthesized onto a microscope slide using spacers to control sample thickness. The film was then cured in an

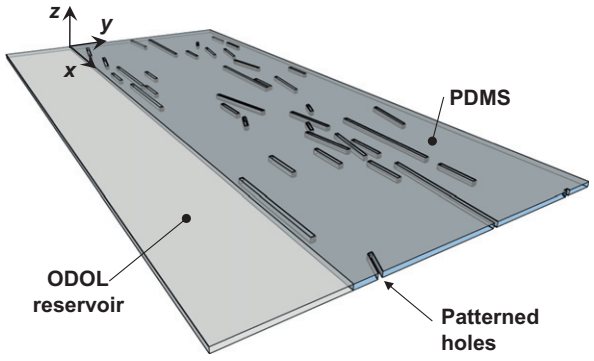

Fig. 2. Schematic of the experiment design: patterned PDMS specimen, ODOL reservoir and reference system.

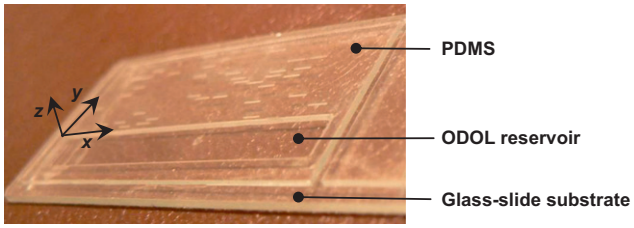

Fig. 3. An actual image of the carved PDMS specimen.

oven at 80 °C for about 3 h. After the PDMS curing, the specimen was patterned using laser ablation to produce a set of holes with pre-established positions and dimensions. Laser ablation was also used to cut the external specimen boundary and to carve the repository for the penetrant. Laser ablation was performed using two instrumentations: i) a commercial VersaLASER VLS3.60 engraving machine with 60 W nominal laser power (maximum) which allowed to carve sample features with dimensions above 200 μm; ii) a research-grade laser ablation system equipped with a femtosecond 800 nm laser beam focused through a microscope objective of 40 ×, which allowed to produce much finer sample features, as small as 10 μm. Most of the specimens used in this work were produced using the VersaLASER machining system.

An actual picture of a specimen mounted onto its glass slide substrate is shown in Fig. 3, where the carved reservoir for ODOL supply and the set of preformed holes can be observed. Notice that thin PDMS walls were used to surround the reservoir in order to prevent liquid ODOL from spilling out. For diffusion experiments, the reservoir was loaded at room temperature with a calculated amount of ODOL, enough to fill it completely. The whole specimen was horizontally placed with the glass slide at the bottom and the PDMS film on the top, on the aluminum plate of a temperature-controlled laboratory oven (± 1 °C). Diffusion was promoted by heating the specimen at specified temperatures, above ODOL melting temperature, under N_2 atmosphere. As the specimen was placed horizontally on the aluminum plate, i.e. normal to the *z*-axis in Fig. 3, gravity had no effect on ODOL transport, which should only occur by diffusion as a consequence of the concentration gradient in *y*-direction. The specimen was checked for ODOL leaking by capillarity between the PDMS film and the glass substrate, but it never occurred due to the excellent contact between PDMS and the glass plate. Over the course of the experiment, particularly for the longest annealing times, the reservoir was refilled with fresh ODOL in order to keep its supply at a constant level.

After pre-established periods of time, the specimen was removed from the oven, cooled back at room temperature, and mounted on the microscope stage for its spectroscopic characterization. The orientation of the specimen on the stage was the same as in the oven, i.e. horizontally, with the PDMS film on top. The optical axis of the microscope was normal to the PDMS surface; this is, coincident with the *z*-axis in Figs. 2 and 3. Using this configuration, the motion of the stage in *x* and *y* directions allowed for the examination of the complete surface of the PDMS film. Two-dimensional Raman maps were constructed point-by-point using a Renishaw Via Reflex spectrometer system equipped with a charge-coupled device (CCD) detector of resolution 1040 × 256 pixels, and coupled to a Leica microscope with a computer-controlled stage. An Ar laser line (514 nm, 50 mW) was used as excitation source in combination with a grating of 2400 grooves/mm. The laser power was kept below 10% to avoid damaging the sample while obtaining good spectra quality. Excitation and collection of light were performed via a Leica objective 50 × (0.75 NA), with the laser in line focus mode. With this configuration, the instrument yields nominal spatial resolutions of 0.5 μm and 6 μm in both the *x* and *y* directions, respectively. Local spectra were recorded using 1 s acquisition time and one accumulation. The focus track option was used in each measurement to properly find the localization of the sample surface, with ± 0.1 μm precision. A typical experiment, consisting in 50 local spectra recorded using the above settings, took about 15 min to complete.

2.2. Computer simulations

The two-dimensional transient mass transport problem was modeled using the Boundary Element Method (BEM). The BEM was selected for the computer simulations due to its simplicity in the problem discretization, limited to the specimen outer boundary and the hole boundaries, and its superior accuracy when compared to other methods to deal with problems presenting strong discontinuities [14], particularly advantageous in our case as we expect strong gradients in the concentration and flux fields in the vicinity of the obstacles. The versatility of the BEM for the numerical evaluation of the barrier properties of flake-filled membranes was demonstrated by Chen and Papathanasiou [6]. Besides, we have recently used BEM for the solution of heat diffusion problems in micro-heterogeneous materials [5,8].

The BEM was used to solve the Fickean transient diffusion problem [14],

$$\nabla^2 C = D\frac{\partial C}{\partial t}\,, \tag{1}$$

where *C* is the ODOL intensity field, *D* is the diffusion coefficient, and ∇^2 is the Laplacian operator. The diffusion coefficient, *D*, associated to the transport of the ODOL in the neat PDMS matrix was set as a constant.

A BEM formulation with time-dependent fundamental solutions was used to solve Eq. (1) [14]. This approach avoids the introduction of domain integrals into the BEM formulation, and so, the "boundary only" characteristic of the method is preserved. On the other hand, the formulation is computational expensive, since every time increment requires to restart the time integration from the initial conditions. To reduce computing time, the implementation of the BEM solver was optimized in two ways: redundant recalculations were reduced by storing the solutions for every time step to be later reused in the integration of subsequent time steps, and the program was coded to run in parallel using OpenMP and FORTRAN. Computations were carried out in a GNU/Linux-based multi-core workstation with two 4-core Xeon CPUs and 16 GB of RAM. The models were discretized using constant elements.

Following the experimental approach, the obstacles to the diffusion were assimilated to holes in the BEM model. The discretization strategy was devised based on preliminary tests performed to explore the model convergence and error [15]. Thus, obstacles were discretized using 5 elements in the thickness and 10 elements in the length, making a total of 30 elements per hole (see Fig. 7(b) and (c) below). The element size for the discretization of the external boundary was set equal to the obstacle thickness. The boundary conditions were set as zero flux along the obstacle (hole) boundaries and along the external boundary, with the only exception of the $y=0$ side, the specimen end coincident with the ODOL reservoir, see Fig. 2. The reservoir was modeled using a Dirichlet boundary condition with a fixed concentration C_0. Internal points were used to compute the concentration profiles within the model domain.

3. Results and discussion

3.1. Diffusion in the homogeneous matrix

We start discussing the spectral characteristics of the components, a first necessary step towards the characterization of ODOL transport in neat PDMS. Fig. 4 shows Raman spectra of pure PDMS and ODOL in the 2700–3100 cm^{-1} region, the base for the spectroscopic characterization. The major peaks can be assigned to the stretching of the C–H bonds of $–CH_2–$ units in ODOL (2845 and 2882 cm^{-1}) and the $–CH_3$ groups of PDMS (2906 cm^{-1}). The very different spectral profiles anticipate good discrimination between components by Raman microscopy.

For the characterization of the transport of ODOL in PDMS, diffusion experiments were carried out using homogeneous non-patterned samples similar to those seen in Fig. 3, with a reservoir for the supply of ODOL molecules at one of its ends. Diffusion in the *y*-direction was promoted by annealing the whole specimen at temperatures above the melting temperature of ODOL. Fig. 5 shows a sequence of Raman spectra measured at different locations along the *y*-axis, this is, at different distances from the ODOL reservoir (see Figs. 2–3), after 6 h of annealing at 100 °C. Spectra were taken at the surface of the specimen, using the focus-track feature of the instrument, in order to avoid attenuation of spectral intensity with depth. It can be seen that the spectral profiles reveal a progressive decrement of the 2882 cm^{-1} peak (assigned to ODOL) with the distance from the ODOL reservoir. This behavior indicates that ODOL has diffused into the PDMS matrix.

Raman spectra were processed by component analysis to obtain individual contributions of ODOL and PDMS to the whole local spectrum. Overall, any of the spectra obtained were effectively reconstructed from a linear superposition of pure ODOL and pure PDMS spectral forms, plus a polynomial function to account for changes in baseline [16]. In this way, the analysis yields the individual contribution of the two species, directly connected with their relative amounts. Fig. 6 shows the ODOL contribution, in the form of ODOL intensity, as a function of the distance from the reservoir for several annealing times. What we refer to as ODOL intensity (A.U.: arbitrary units) is the actual intensity per sampled volume, which is a measure of ODOL concentration in mass per unit volume. In the initial condition, ODOL is absent in the PDMS matrix, as it can be seen from the ODOL intensity profile reported for zero time in Fig. 6(a). Then, with time, ODOL diffuses and progressively increases its concentration in the matrix; see Figs. 6(b) to (d). It can be seen that the intensity data

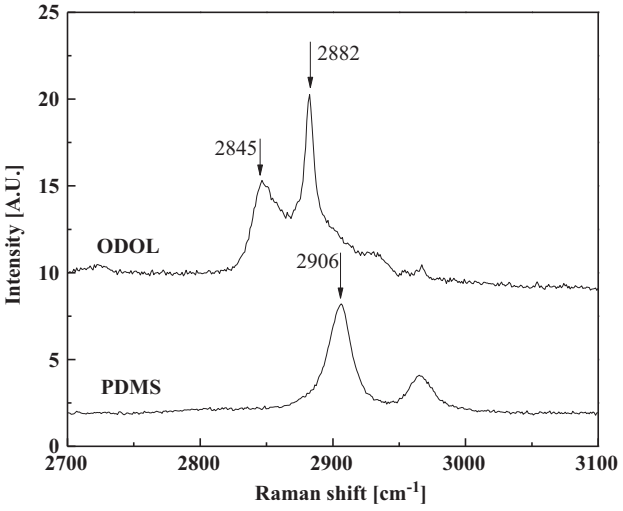

Fig. 4. Raman spectra of ODOL and PDMS individual components.

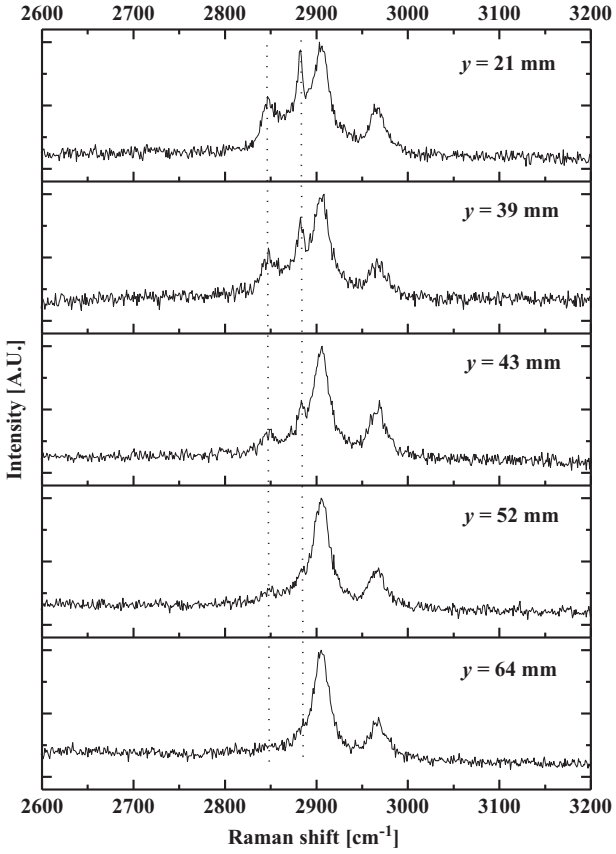

Fig. 5. Raman spectra at different distances from the ODOL reservoir after 6 h of annealing at 100 °C.

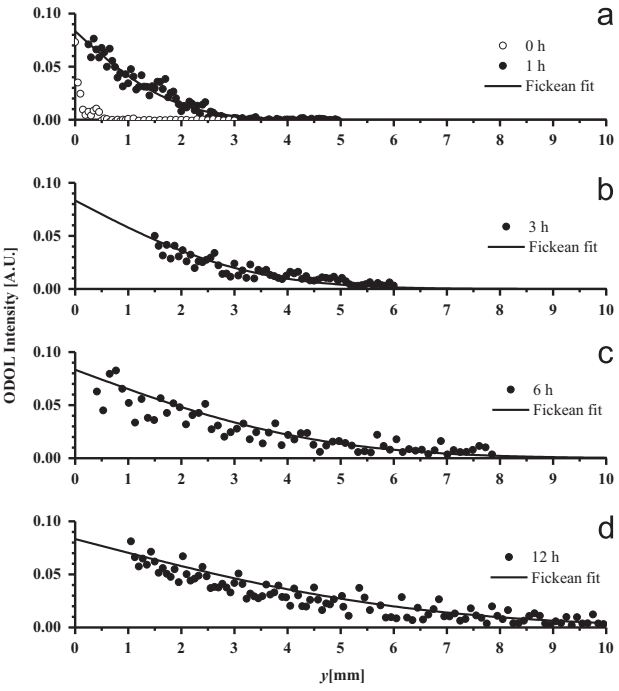

Fig. 6. Profiles of ODOL intensity per sampled volume in homogeneous PDMS at 100 °C.

are somewhat noisy; this behavior is attributed in a major part to the crystallization of ODOL at room temperature on the PDMS surface, a phenomenon also observed in diffusion of alkanethiols in a similar matrix [17].

We tested the validity of a simple Fickean diffusion model to fit the data and to characterize the whole process through a single transport coefficient, D_0. The Fickean character of ODOL diffusion was first confirmed by plotting the data in terms of the characteristic variable $y/(4t)^{0.5}$, with t being the annealing time [18]. We found that the whole set of data could be superimposed onto a single curve. Next, we fit those data to a one dimensional Fickean model with a constant diffusion coefficient, subjected to boundary conditions of semi-infinite supply [18]. We assumed that the ODOL concentration for the repository, C_0, remained constant in time, this is, the repository was supposed to be large enough to supply as much ODOL as it was demanded by the diffusion process. The lines in Fig. 6 represent the Fickean model predictions for the best fit of the diffusion coefficient, $D_0=3.3\ (\pm 0.1)\times 10^{-6}$ cm^2/s. On the other hand, the value for $C_0=0.083\ (\pm 0.001)$, in mass per unit volume, resulted from the measurement of the ODOL intensity per sampled volume in the proximity of the reservoir. Overall, we see that the fitting is satisfactory. The value for D_0 resulting from the analysis compares very well with that found for alkanethiols transport in a similar matrix at room temperature, 5×10^{-7} cm^2/s [17]. In summary, the experimental data confirms that diffusion of ODOL in PDMS at 100 °C is essentially Fickean, at least up to diffusion times of 12 h.

3.2. Diffusion through the model material with obstacles

Fig. 7 shows an actual picture of the specimen used for the diffusion experiments of the model material with obstacles and its corresponding BEM model. The obstacles in the form of holes had a nominal width $a=200$ μm and a length $2d=2000$ μm. They were placed with its length parallel to the x-axis; this is, perpendicular to the overall diffusion direction, and distributed randomly throughout the specimen. The volume fraction of obstacles ϕ was set 0.03. This setup constitutes a rather challenging case, as the small values of the obstacle aspect ratio, $\alpha=2d/a$, and relatively low amount of obstacles, anticipate minor changes in the overall (or apparent) diffusivity of the whole specimen, D_{App}. For instance, the model due to Lape and Cussler predicts that the overall diffusivity of this material is about 80% that of the pure matrix [1]. As a consequence, the ODOL concentration profiles should not deviate significantly from those of the homogeneous matrix, except by local perturbations in the zones near the obstacles. The capture of these perturbations justifies the local Raman measurements and the high-resolution BEM simulations. On the other hand, there are the effects of these local perturbations, combined for all the obstacles in the sample, that determine the macroscopic specimen response, D_{App}, as it is calculated in conventional permeability experiments.

The methodology applied for confocal Raman characterization was similar to that described in the previous section for the homogeneous matrix. ODOL intensity profiles along the specimen were produced from the Raman spectra monitored along a set of lines in the directions $x_1=14.8$ mm, $x_2=20$ mm, and $x_3=30$ mm; and $y_1=2$ mm, $y_2=3$ mm, and $y_3=4$ mm, see Fig. 7(b). Particular interest was put to probe the concentration fields nearby the obstacles.

The BEM model discretization is depicted in Fig. 7(b), while Fig. 7(c) is a close-up with the discretization of an obstacle, see the Computer Simulations section for the description of the discretization strategy. The concentration of the ODOL reservoir was set $C_0=0.083$, the same value used in the earlier Fickean fits, via the Dirichlet boundary condition along the side $y=0$. The

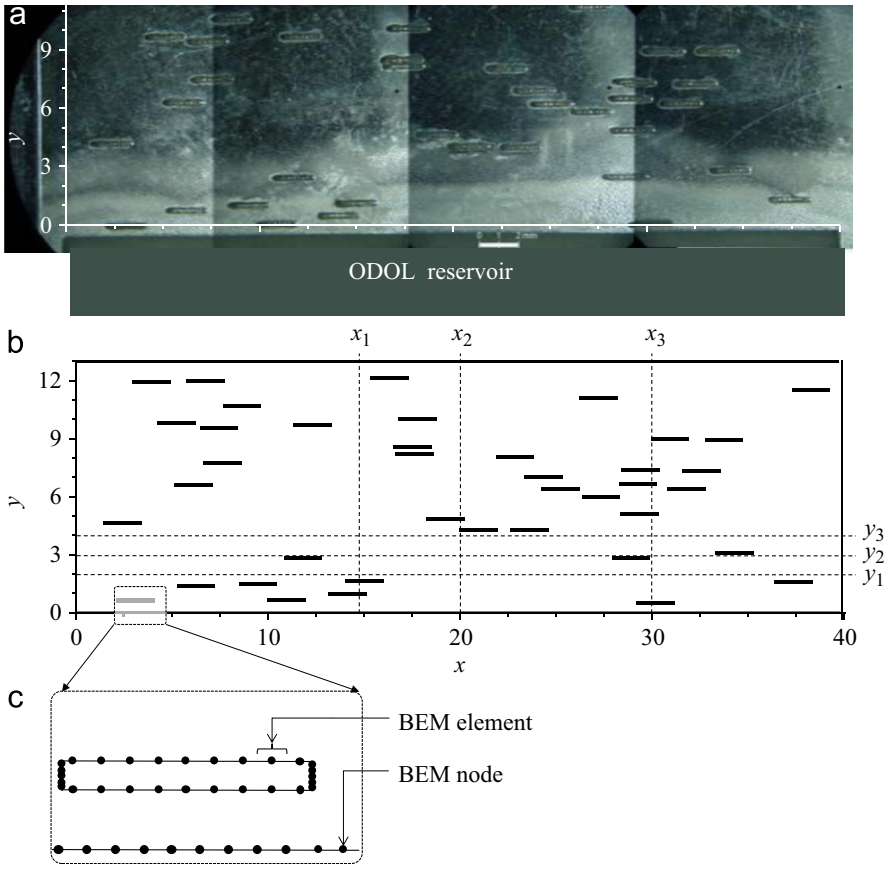

Fig. 7. Specimen with barriers to diffusion: (a) actual picture (whitish marks are due to ODOL diffusion); (b) BEM model and (c) discretization details. The dotted lines indicate directions of mappings for the Raman microscopy. Dimensions are in mm.

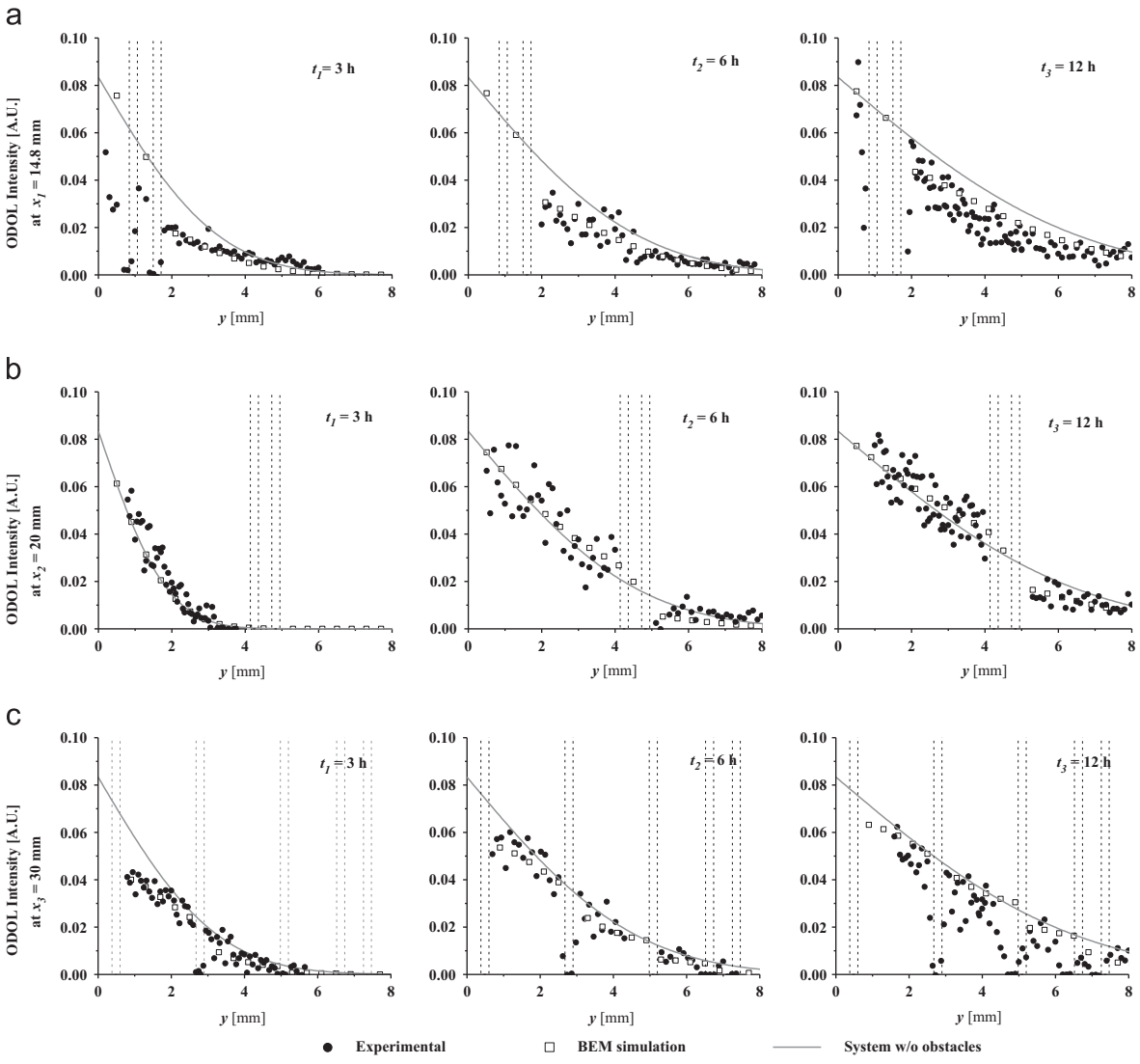

Fig. 8. Time evolution of the profiles of ODOL intensity per sampled volume along paths in the direction of the macroscopic diffusion: (a) x_1=14.8 mm; (b) x_2=20 mm; (c) x_3=30 mm. Data from Raman microscopy analyses (filled symbols), BEM models (open symbols) and a Fickean analytical model without obstacles (dotted lines).

diffusion coefficient for the simulations was set to $D=3.3\times10^{-6}\,cm^2/s$, in accordance with the mean value of D_0, that obtained for the diffusion experiments of ODOL in pure PDMS reported in the previous section. The value for the time increment, Δt, was set to 120 s. The internal points for the computation of the concentration profiles were placed to define lines in the directions x_i and y_i specified in experimental setup, see Fig. 7(b). The distance between the internal points was set equal to 400 μm.

Fig. 8 shows the evolution with time (t_i=1 h, 6 h and 12 h) of the ODOL intensity profiles along the specimen length, for the positions x_1=14.8 mm, x_2=20 mm and x_3=30 mm. The closed symbols correspond to the experimental data from the Raman measurements. Once again, the oscillations observed in the experimental results are attributed to the crystallization of ODOL at the temperature of the micro-spectroscopic analysis (25 °C). The results of the BEM simulations are shown in open symbols. There are also included in the plots the analytical solution of Fick's law for a system without obstacles (continuous lines). The vertical dotted lines indicate the position of the preformed holes, in correspondence with Fig. 7(b). The differences between numerical models and experimental data for all the results in Fig. 8 were assessed via the Normalized Root Mean Square Errors (NRMSE), as summarized in Table 1. The NRMSE was computed for the discrepancies of both, the BEM results and the Fickean analytical solution, with respect to the experimental measurements, using in every case the maximum spread of the experimental results as normalization factor.

Table 1
Discrepancies of the BEM results and the Fickean analytical solution with respect to the experimental measurements. Labels (a), (b) and (c) used in the identification of the paths make reference to those of Fig. 8.

Path (mm)	Time (h)	NRMSE BEM	NRMSE Fick
(a) x_1=14.8	3	0.2063	0.3613
	6	0.1330	0.2755
	12	0.1480	0.3592
(b) x_2=20	3	0.1044	0.0983
	6	0.0934	0.1050
	12	0.0701	0.0829
(c) x_3=30	3	0.0543	0.1943
	6	0.0768	0.1551
	12	0.1705	0.2292

We see from Fig. 7, that two holes are placed at the very beginning of the diffusion path along x_1=14.8 mm, at positions

$y=1$ mm and 1.5 mm. Their influence on the concentration field is clearly reflected in Fig. 8(a), as shown by the discontinuities observed in the ODOL intensity profiles at the positions coincident with the barriers. The concentration of ODOL predicted ahead of the obstacles by the Fickean model, which ignores the presence of the obstacles, is much higher than that observed experimentally. In contrast, the barrier effect to the ODOL diffusion is well captured by both, the experimental and BEM results. In this sense, the results in Table 1 show that the discrepancies in terms of NRMSE between the Fickean model and the experimental measurements are between 1.7 and 2.4 times larger than those between experiments and BEM results.

The distribution of the obstacles along the path $x_2=20$ mm is different to that discussed for x_1, as the holes are now mostly located in the central third of the specimen length, see Fig. 7(b). In accordance to this, the obstacles produced no effects on the ODOL profiles for the observation at $t_1=3$ h in Fig. 8(b), and the experimental results are well predicted by both, Fickean and BEM models; see in Table 1 that the discrepancies for both sets of results are nearly the same, within 2%. On the other hand, the effects of the obstacles operate in later stages of the experiment, $t_2=6$ h and $t_3=12$ h, where the penetrant has reached the obstacles, giving rise to discontinuities in the ODOL intensity profiles. Both, Fickean and BEM solutions yield similar results, with discrepancies with respect to the experiments in the range 7–10%, see Table 1.

The path at $x_3=30$ mm has holes distributed along the complete sample length. Consequently, the discontinuities due to the obstacles on the concentration profiles can be appreciated at all the observation times. This case results in the worst performance for the Fickean model. As seen in Table 1, the discrepancies of the Fickean model predictions and the experimental measurements are 1.35–3.6 times larger than those performed by BEM. Finally, it is worth to mention that the above results confirm the behavior anticipated earlier for the overall ODOL profiles along the specimen length: the low volume fraction of obstacles has mainly local effects. The ODOL profiles along the specimen can be assimilated to that of the homogeneous matrix with perturbations in the neighborhood of the obstacles.

Fig. 9 shows results for the ODOL concentrations profiles across the specimen, at different y positions, $y_1=20$ mm, $y_2=30$ mm and $y_3=40$ mm, and for several diffusion times. Raman data are represented by solid symbols, open symbols correspond to BEM simulations and the continuous horizontal lines are the predictions of the Fickean model for the homogeneous case. It can be seen that, due to the presence of obstacles, the diffusion front resulting from the experiments and the BEM model is not constant, as it is the case of the homogeneous Fickean solution. Note that in these cases, the monitored paths do not intersect the obstacles, so the profiles are continuous, with peaks and valleys that correspond to "windows" between the obstacles and the "shield" effect of the obstacles, respectively. Remarkably, Fig. 9(b, c) shows that the ODOL concentration in the region $x=20$–25 mm is predicted to be above that calculated from the Fickean model. From Fig. 7(b), it can be observed that the measurement line is located right behind two adjacent holes, so BEM is correctly predicting the accumulation of ODOL that cannot diffuse due to the presence of the obstacle. As for the previous set of results, BEM predictions are in better agreement with the experimental data than those of the Fickean model, as reflected by improvements in discrepancies up to 65%.

In summary, it can be concluded from the above results that the BEM predictions are in better agreement with the experimental data that the simple Fickean solution. NRMSE in the range 0.05–0.21 for BEM solutions are remarkably good, considering we are capturing, experimental and numerically, local and relatively small perturbations in the ODOL intensity field. In this sense, it is important to consider that due the high gradients in the vicinity of the obstacles, the ODOL intensity measurements are very sensitive to position, that is, small errors in positioning may lead to rather large variations in ODOL intensity.

We end the paper with a comment about the feasibility of using the presented experimental setup to obtain global measurements, representative of the geometry of the whole specimen, besides the local analysis shown earlier. For instance, the kind of experimental data shown in Fig. 9 can serve as a basis for the determination of a global or apparent diffusivity, as the integrated profile along the complete diffusion front is a measure of the amount of mass that has diffused up to that time, for this position. A representation of the mass diffused versus square root of time should yield a linear plot whose slope is related with the apparent diffusion coefficient of the heterogeneous system, D_{App} [18]. Compared with the values of D_0 that characterize the homogeneous matrix, the analysis yields the relative diffusivity D_{App}/D_0, a variable used to describe the reduction of permeability as a function of system micro/nanostructure in most of the fundamental models in the literature.

4. Conclusions

We have presented an experimental setup conceived for the study and monitoring of barrier effects in materials with model

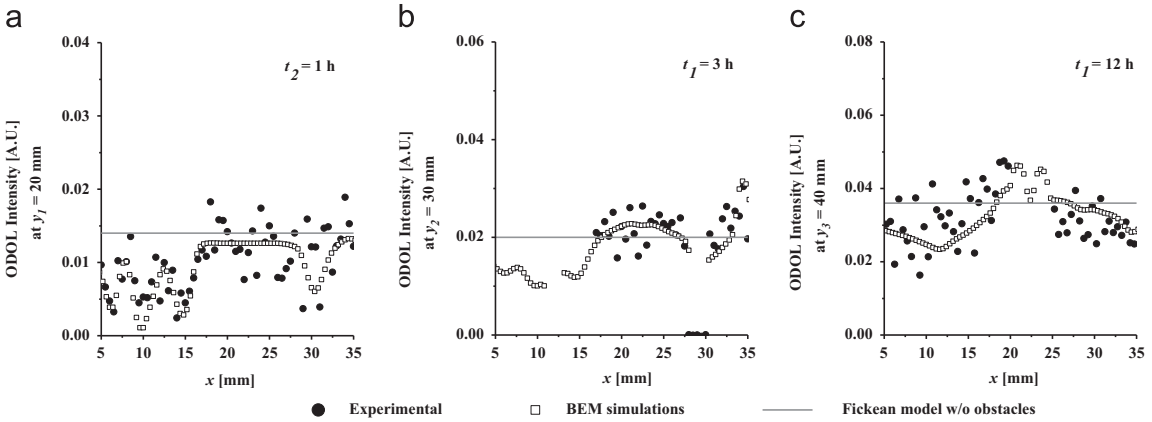

Fig. 9. Intensity per sampled volume ODOL profiles across the specimen for selected y-positions and times. Data obtained by Raman microscopy and computed using BEM and the Fickean diffusion model. Data from Raman microscopy analyses (filled symbols), BEM models (open symbols) and a Fickean analytical model without obstacles (dotted lines).

microstructures consisting in a homogeneous matrix with impenetrable obstacles. Experiments were performed using PDMS specimens with a controlled pattern of randomly distributed laser-ablated microscopic slender holes that mimic the obstacles to the diffusion. Laser ablation was found very efficient at producing any type of holes morphology with perfectly controlled positions and orientations, and with dimensional features ranging from 1000 μm up to 10 μm. In this way, materials with well-defined morphologies could be synthesized in basically two steps consisting in PDMS curing followed by laser carving. The experimental system designed to monitor mass transport, based on confocal Raman microscopy, allowed the non-invasive monitoring a long chain alcohol diffusion (ODOL) through the generated morphologies, thus providing valuable experimental data on the alterations of the penetrant concentration fields caused by the obstacles.

Diffusion of ODOL in the homogeneous PDMS matrix was Fickean. ODOL diffusion was also characterized in a matrix with a relatively low amount ($\phi=0.03$) of moderately elongated obstacles ($\alpha=10$). The experiments showed that the carved holes acted as obstacles for ODOL diffusion, altering the concentration fields nearby the holes. Details at local level were well captured by the experimental technique, despite the relatively minor overall barrier effect predicted for the studied case. Numerical simulations for the process were performed via high-resolution Boundary Element analysis, based only on the geometrical and topological details of the material microstructure and on a transport coefficient for ODOL in neat PDMS, which was independently determined. Overall, we found that BEM simulations were in excellent agreement with Raman results, which is particularly remarkable given that no fitting parameters, typical of theoretical models, were necessary to carry out the calculations.

The proposed experimental and numerical tools have excellent potential as means for the verification and validation of theoretical models for mass transport through heterogeneous systems. Model materials microstructures with obstacles of arbitrary shape, positions and orientations can be numerically modeled and fabricated for the experimental testing. The spatial discrimination of the confocal microscopy appears not only suitable to perform local analysis but also global measurements. This versatility allows tackling not only the analysis of heterogeneous microstructures as it has been the case in this work, but also new families of advanced materials such as for instance, functionally graded microstructures.

Acknowledgements

We would like to thank financial support from Agencia Nacional de Promoción Científica y Tecnológica via PICT10–284 (J. P. Tomba) and PICT07–1154 (A. P. Cisilino). The authors would like to thank Drs. G. Bilmes and G. Torchia from Centro de Investigaciones Ópticas at the Universidad Nacional de La Plata (Argentina) for valuable discussions about laser ablation experiments.

Nomenclature

a	obstacle width
d	obstacle half-length
C_0	ODOL concentration in the reservoir
D_0	experimentally determined diffusion coefficient of the homogeneous matrix
D_{App}	apparent diffusion coefficient of the specimen
D	diffusion coefficient used in BEM simulations
t	annealing time

Greek symbols

α	obstacle aspect ratio, $2d/a$
ϕ	volume fraction of obstacles
Δt	time increment in BEM simulations

References

[1] N.K. Lape, E.E. Nuxoll, E.L. Cussler, Polydisperse flakes in barrier films, J. Membr. Sci. 236 (2004) 29–37.
[2] A.D. Drozdov, J.deC. Christiansen, R.K. Gupta, A.P. Shah, Model for anomalous moisture diffusion through a polymer–clay nanocomposite, J. Polym. Sci. B: Polym. Phys. 41 (2003) 476–492.
[3] G. Choudalakis, A.D. Gotsis, Permeability of polymer/clay nanocomposites: a review, Eur. Polym. J. 45 (2009) 967–984.
[4] R.K. Bharadwaj, Modeling the barrier properties of polymer-layered silicate nanocomposites, Macromolecules 34 (2001) 9189–9192.
[5] M. Dondero, A.P. Cisilino, J.M. Carella, J.P. Tomba, Effective thermal conductivity of functionally graded random micro-heterogeneous materials using representative volume element and BEM, Int. J. Heat Mass Transfer 54 (2011) 3874–3881.
[6] X. Chen, T.D. Papathanasiou, Barrier properties of flake-filled membranes: review and numerical evaluation, J. Plast. Film Sheeting 23 (2007) 319–346.
[7] A.A. Gusev, H.R. Lusti, Rational design of nanocomposites for barrier applications, Adv. Mater. 13 (2001) 1641–1643.
[8] M. Dondero, A.P. Cisilino, J.P. Tomba, Numerical design of random micro-heterogeneous materials with functionally-graded effective thermal conductivities using genetic algorithms and the fast boundary element method, Comput. Model. Eng. Sci. 78 (2011) 225–246.
[9] T.I. Zohdi, P. Wriggers, Introduction to Computational Micromechanics, Lecture Notes in Applied and Computational Mechanics, First edition, Springer-Verlag, Berlin, 2005.
[10] V.G. Kouznetsova, Computational Homogenization for the Multi-Scale Analysis of Multi-Phase Materials, PhD thesis, Eindhoven Technische Universiteit Eindhoven, 2002.
[11] Q. Liu, E.L. Cussler, Barrier membranes made with lithographically printed flakes, J. Membr. Sci. 285 (2004) 56–67.
[12] R.R. Gattass, E. Mazur, Femtosecond laser micromachining in transparent materials, Nat. Photonics 2 (2008) 219–225.
[13] Y. Xia, G.M. Whitesides, Soft lithography, Angew. Chem. Int. 37 (1998) 550–575.
[14] L.C. Wrobel, The Boundary Element Method, Potential Problems, John Wiley & Sons, Chichister, UK, 2002.
[15] D. Santiago, M. Dondero, A.P. Cisilino, S. Urquiza, BEM Solver Implementation Within a Discrete Methods Application Framework, XI Pan-American Congress of Applied Mechanics, American Academy of Mechanics, Foz do Iguacu, 2010.
[16] J.P. Tomba, E. de la Puente, J.M. Pastor, Calculation of polymer blend compositions from Raman spectra: a new method based on parameter estimation techniques, J. Polym. Sci. Part B: Polym. Phys. 38 (2000) 1013–1023.
[17] T.E. Balmer, H. Schmid, R. Stutz, E. Delamarche, B. Michel, N.D. Spencer, H. Wolf, Diffusion of alkanethiols in pdms and its implications on microcontact printing, Langmuir 21 (2005) 622–632.
[18] J. Crank, The mathematics of diffusion, Oxford University Press, USA, 1980.